

Polymorphic Layered MoTe_2 from Semiconductor, Topological Insulator, to Weyl Semimetal

Raman Sankar,^{*,†,‡,§,||,∇} G. Narsinga Rao,[‡] I. Panneer Muthuselvam,^{†,‡,⊥} Christopher Butler,[§] Nitesh Kumar,[#] G. Senthil Murugan,[‡] Chandra Shekhar,[#] Tay-Rong Chang,^{||} Cheng-Yen Wen,[⊥] Chun-Wei Chen,[⊥] Wei-Li Lee,[†] M.-T. Lin,[§] Horng-Tay Jeng,^{†,||} Claudia Felser,[#] and F. C. Chou^{*,†,‡,§,||,∇}

[†]Institute of Physics, Academia Sinica, Taipei 10617, Taiwan

[‡]Center for Condensed Matter Sciences, [§]Department of Physics, and [⊥]Department of Materials Science and Engineering, National Taiwan University, Taipei 10617, Taiwan

[#]Max Planck Institut für Chemische Physik fester Stoffe, Nöthnitzer Straße, 01187 Dresden, Germany

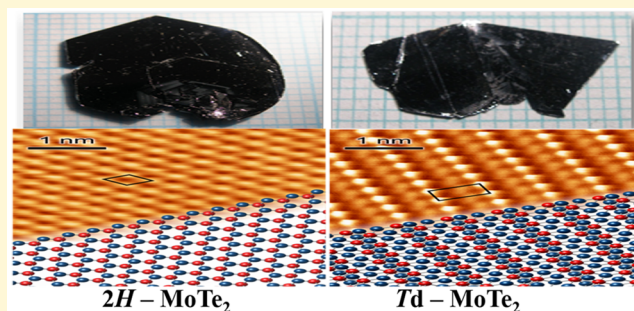
^{||}Department of Physics, National Tsing Hua University, Hsinchu 30013, Taiwan

^{||}National Synchrotron Radiation Research Center, Hsinchu 30076, Taiwan

[∇]Taiwan Consortium of Emergent Crystalline Materials, Ministry of Science and Technology, Taipei 10622, Taiwan

Supporting Information

ABSTRACT: Large size (~ 2 cm) single crystals of layered MoTe_2 in both $2H$ - and $1T'$ -types were synthesized using TeBr_4 as the source of Br_2 transport agent in chemical vapor transport growth. The crystal structures of the as-grown single crystals were fully characterized by X-ray diffraction, Raman spectroscopy, scanning transmission electron microscopy, scanning tunneling microscopy (STM), and electrical resistivity (ρ) measurements. The resistivity $\rho(T)$, magnetic susceptibility $\chi(T)$, and heat capacity $C_p(T)$ measurement results reveal a first order structural phase transition near ~ 240 K for $1T'$ - MoTe_2 , which has been identified to be the orthorhombic Td -phase of MoTe_2 as a candidate of Weyl semimetal. The STM study revealed different local defect geometries found on the surface of $2H$ - and Td -types of MoTe_6 units in trigonal prismatic and distorted octahedral coordination, respectively.



INTRODUCTION

The two-dimensional (2D) layered transition metal dichalcogenides (TMDs), MX_2 ($M = \text{Ta}, \text{Mo},$ or W and $X = \text{Se}, \text{S},$ or Te), have attracted significant attention due to their rich physical properties including superconductivity, large thermoelectric effect, and anomalous magnetoresistance.^{1–5} These 2D materials have shown promising potential for next-generation devices as an alternative to graphene as a 2D monolayer material.^{6,7} In search of materials having both a band gap like a typical semiconductor and a high charge carrier mobility like graphene, the recently demonstrated MoTe_2 -based high mobility device opened a new area for future applications.⁸

The recent theoretical prediction and following discovery of WTe_2 as a topological type-II Weyl semimetal⁹ with extremely large magnetoresistance⁵ have triggered extensive attention to uncover the origin of these intriguing emerging physical properties identified in TMDs, which arise from rich variations of intralayer packing of MX_6 octahedral or trigonal prismatic units and interlayer stacking via van der Waals (vdW) interlayer interactions.^{10,11} The two most common structures of TMDs are the $2H$ -type (space group $P6_3/mmc$ with MX_6 in trigonal

prismatic coordination) and the $1T$ -type (space group $P\bar{3}m1$ with edge-shared MX_6 in octahedral coordination).¹⁰ In addition to the common $2H$ -type structure, MoTe_2 has also been found in a variation of $1T$ -type (α), namely the $1T'$ -type (β), which is composed of buckled layers of edge-sharing MoTe_6 octahedra in monoclinic symmetry of space group $P2_1/m$.^{12–14} Although the name $1T'$ -type has been discussed theoretically in parallel to those of $1T$ - and $1H$ -types by assuming there is one layer per unit cell,¹⁵ the experimentally identified two layers per unit cell following the space group $P2_1/m$ operation suggests that the correct categorization for the recently discussed $1T'$ -type should be named $2T'$ -type following the convention of TMDs.¹⁶ So as not to be confused with those discussed in recent publications, we will continue to use the term $1T'$ in this paper.

Recent theoretical investigations showed that the separation of Weyl points as well as the length of a Fermi arc can be

Received: October 12, 2016

Revised: December 19, 2016

Published: December 20, 2016

adiabatically tuned as a function of Mo-doped WTe_2 ,¹⁷ and the orthorhombic Td phase of pristine MoTe_2 also possesses type-II Weyl nodes,¹⁸ which have much larger Weyl node pair separations than those found in WTe_2 .^{9,18} Hence, Td - MoTe_2 is expected to provide more convincing experimental evidence via angle-resolved photoemission spectroscopy compared to that of WTe_2 . On the basis of the transport studies of single crystal $\beta(1T')$ - MoTe_2 in the literature, the hysteretic behavior of resistivity near ~ 247 K corresponds to the structural phase transition from the $1T'$ -type to the low temperature orthorhombic Td -phase,^{14,19} although a recent investigation focusing on the few-layered $1T'$ - MoTe_2 did not confirm the Td phase existence.²⁰

$1T'$ - MoTe_2 and Td - MoTe_2 phases differ in their β angles, i.e., the former is monoclinic with $\beta = 93.9^\circ$ slightly deviated from a right angle, but the latter is orthorhombic.¹⁹ Surprisingly, this small distortion makes a crucial difference in the symmetry-induced electronic property change. Although the monoclinic $1T'$ phase has both time-reversal and inversion symmetry, the Td phase MoTe_2 of missing inversion symmetry becomes a promising candidate for the investigation of Weyl fermions.¹⁸

It is clear that the growth of temperature-sensitive polymorphic single crystals of MoTe_2 is a challenge. Here, with the aim of growing large and high quality MoTe_2 single crystals of controlled structure types, we have demonstrate the successful growth of polymorphic single crystals using a novel chemical vapor transport (CVT) method that involves a mixture of Mo and TeBr_4 as the precursor, where TeBr_4 decomposed at 420°C becomes the natural source of Br_2 as the transport agent in the CVT growth. By controlling the temperature profile of the source, large crystals (~ 2 cm) of MoTe_2 have been grown successfully in less than a week. Details of the CVT growth method as well as a comprehensive characterization of the as-grown single crystals are presented, including X-ray diffraction (XRD), Raman spectroscopy, scanning transmission electron microscopy (STEM), scanning tunneling microscopy (STM), and transport measurements.

EXPERIMENTAL SECTION

Synthesis and Crystal Growth. The chemical vapor transport method was employed using TeBr_4 as Br_2 source, which acts as the transport agent and allows an effective and faster vapor transport to produce the necessary supersaturation of the expected final product. A three-zone muffle furnace was fabricated for this purpose, having typical temperature profiles for the growth of single crystals of $2H$ - MoTe_2 and $1T'$ - MoTe_2 , as shown in Figure S1. A stoichiometric amount of $\text{Mo}/\text{Te} = 1:2$ (6N purity for Te and 5N for Mo) was sealed into an evacuated quartz ampule and heated for 2 days at 750°C . Approximately 10 g of the prereacted MoTe_2 powder was placed together with a variable amount of TeBr_4 (purity 4N) (120 mg) at one end of the silica ampule (length of 40 cm with inner diameter of 1.8 cm and outer diameter of 2.0 cm). Bromine concentration in the range of 2.6–3.7 mg was yielded sufficiently from ~ 5 mg of TeBr_4 per cm^3 , which provided high transport rates of nearly 150 mg per day. All preparation steps before the quartz tube evacuated flame sealing were carried out in an argon-filled glovebox of oxygen, and the water level was kept below ~ 1 ppm. The loaded ampule was evacuated and flame sealed before loading into the tube furnace for CVT growth. For the growth of $1T'$ - MoTe_2 single crystals, the end of the ampule containing the prereacted material was held at 1050°C , and the growth end was maintained at a temperature near 950°C with a temperature gradient near $2.5^\circ\text{C}/\text{cm}$ for a week. Shiny $1T'$ - MoTe_2 single crystals of sizes up to $17 \times 10 \times 2$ mm³ were obtained, as shown in the inset of Figure 1(a). For the growth of $2H$ - MoTe_2 single crystals, the prereacted material was held at 800°C , and the crystals were grown at the end

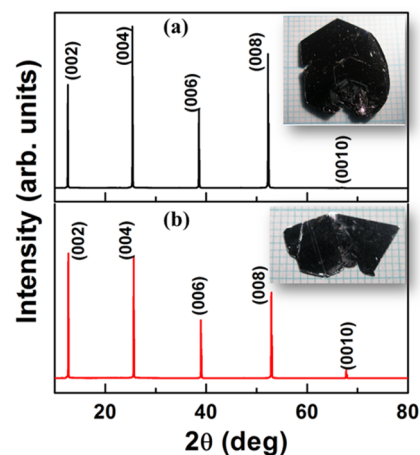


Figure 1. X-ray diffraction patterns of (a) $2H$ - and (b) $1T'$ - MoTe_2 single crystals taken from the platelike pieces of preferred (001) orientation. The as-grown single crystal samples are shown in the insets.

maintained at a temperature of 750°C with a temperature gradient near $1.25^\circ\text{C}/\text{cm}$ for approximately a week. Shiny $2H$ - MoTe_2 single crystals of sizes up to $21 \times 16 \times 2$ mm³ were obtained, as shown in the inset of Figure 1(b).

The crystal structure and phase purity of the samples were checked by synchrotron X-ray powder diffraction (SXRD) using a wavelength of $\lambda = 0.619927$ Å (BL01C2, NSRRC, Taiwan). Raman spectroscopy was performed in the backscattering configuration using 632 nm excitation lasers. The field-cooled (FC) and zero-field-cooled (ZFC) magnetization curves were measured in a commercial vibrating sample magnetometer (VSM, Quantum Design, USA) in the presence of an applied magnetic field of 10 kOe. The heat capacity (C_p) and transport measurements were carried out using the physical properties measurement system (PPMS, Quantum Design, USA).

RESULTS AND DISCUSSION

The room-temperature SXRD patterns of the pulverized as-grown MoTe_2 single crystal are shown in Figure S2. All diffraction peaks for single crystals grown at the low temperature (750°C) profile can be indexed with space group $P6_3/mmc$ (No. 194) of hexagonal $2H$ -type,¹² whereas the crystals grown at high temperature (950°C) can be indexed with space group $P2_1/m$ (No. 11) of monoclinic $1T'$ -type at room temperature.¹³ In addition, the low temperature ($T = 200$ K) diffraction peaks are indexed with space group $Pmn2_1$ (No. 31) of orthorhombic Td - MoTe_2 . The refined lattice parameters are listed in Table 1 and found to be consistent with the values reported in the literature.^{12,13,21–25} The diffraction patterns for the as-grown single crystals with planes of preferred orientation of (00 l) reflections only are shown in Figure 1.

$2H$ - MoTe_2 crystallizes in a layer-type structure with Mo atoms surrounded by six Te atoms in a trigonal prismatic coordination similar to that of $2H$ - MoS_2 .¹² $2H$ - MoTe_2 has been characterized by a stacking sequence of $\text{XyXYxY}\cdots$ (X,Y: Te atom; y,x: Mo atom) with all monatomic planes in 2D hexagonal close packing,²⁶ as shown in Figure 2(a). Alternatively, the $2H$ -type is easier to describe using the face-sharing hexagonal close packing of trigonal prismatic MoTe_6 units in each layer, and these layers are held together by the weak van der Waals force that gives rise to the quasi-two-dimensional character, as shown in Figure 2(d). On the other hand, $1T'$ - MoTe_2 could be viewed as a distortion of the typical $1T'$ -type with layers composed of edge-sharing MoTe_6 -

Table 1. Crystal Structures and Lattice Parameters of MoTe₂ Single Crystals

crystal type	space group	<i>a</i> (Å)	<i>b</i> (Å)	<i>c</i> (Å)	angle
2 <i>H</i> -MoTe ₂	<i>P</i> 6 ₃ / <i>m</i> <i>m</i> <i>c</i>	3.4474(2)	3.4474(2)	9.3528(3)	$\beta = 90^\circ; \gamma = 120^\circ$
1 <i>T'</i> -MoTe ₂	<i>P</i> 2 ₁ / <i>m</i>	3.4692(4)	6.3348(4)	13.8835(2)	$\beta \approx 93.9^\circ$
<i>Td</i> -MoTe ₂	<i>P</i> <i>m</i> <i>n</i> 2 ₁	3.4783(4)	6.3563(2)	13.8935(2)	$\beta = 90^\circ$

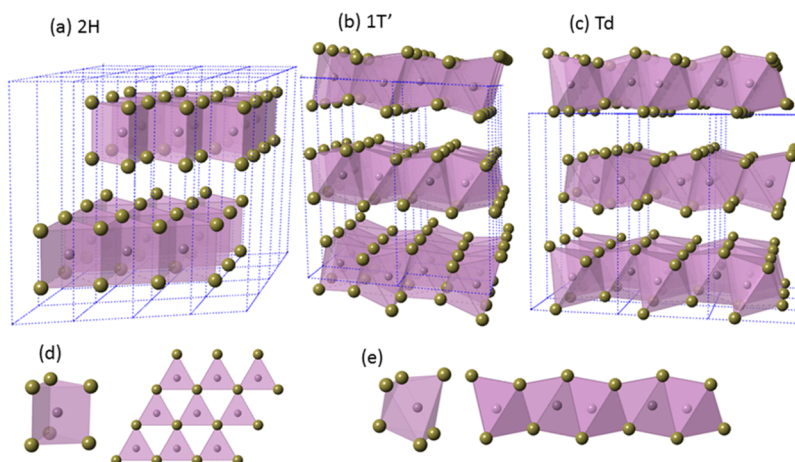


Figure 2. Crystal structures of (a) 2*H*-MoTe₂, (b) 1*T'*-MoTe₂, and (c) *Td*-MoTe₂; the MoTe₆ unit has a trigonal prismatic coordination for 2*H* and a distorted octahedral coordination for 1*T'* and *Td*. MoO₆ coordination and projection views for 2*H*-MoTe₂ along the [001] and *Td*-MoTe₂ along the [100] directions are shown in (d) and (e), respectively.

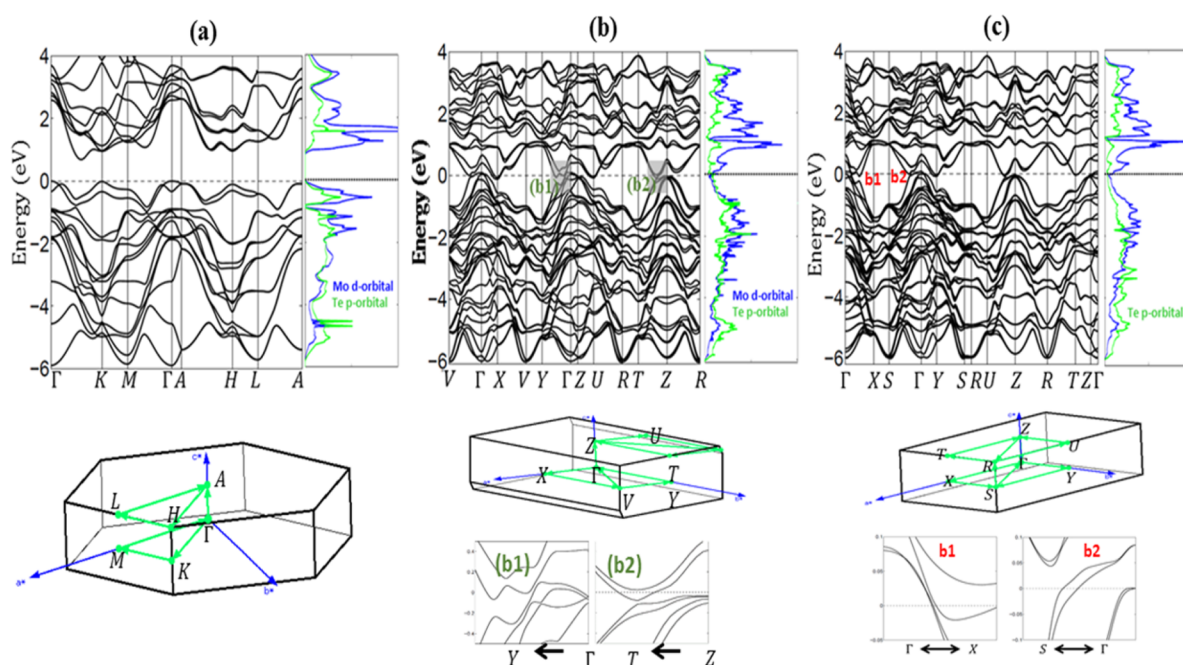


Figure 3. Band structures and density of states of (a) 2*H*-MoTe₂, (b) 1*T'*-MoTe₂, and (c) *Td*-MoTe₂. Blue and green lines indicate the Mo *d*-orbital and Te *p*-orbital, respectively. The corresponding first Brillouin zones (BZ) of all samples are shown below. The insets (b1) and (b2) of 1*T'*-MoTe₂ are enhanced images around E_F , which show a well-defined continuous energy gap throughout the whole BZ. The insets (b1) and (b2) of *Td*-MoTe₂ show the enhanced band structure around E_F , which shows a pair of Weyl points along Γ -*X* and is fully gapped along the Γ -*S* direction.

octahedra, which is demonstrated by the monoclinic distortion of $\beta \approx 93.9^\circ$ from the original hexagonal lattice, as shown in Figure 2(b). The distortion from 1*T* to 1*T'* not only breaks the in-plane hexagonal symmetry with the added mirror symmetry, the Te monolayers above and below the Mo monolayer also rearrange in a zigzag deviation along the *z*-direction relative to that of the flat Mo monolayer. The low temperature orthorhombic *Td*-MoTe₂ phase differs from the 1*T'*-MoTe₂

phase by a small deviation from the right angle for β , i.e., the monoclinic angle of 1*T'* has a slightly larger ($\beta = 93.55^\circ$) than that of $\beta = 90^\circ$ for *Td* with orthorhombic symmetry, as shown in Figure 2(c). It should also be noted that the structure symmetry of the 1*T'*-WTe₂ reported in the literature is identical to the *Td*-MoTe₂ phase instead of the 1*T'*-MoTe₂.²⁷

The electronic structure of 2*H*-MoTe₂, 1*T'*-MoTe₂, and *Td*-MoTe₂ were calculated using a $30 \times 30 \times 6$ and $8 \times 16 \times 4$

Monkhorst–Pack k -mesh over the Brillouin zone (BZ), respectively, as shown in Figure 3. The first-principles calculations were based on the generalized gradient approximation (GGA)²⁸ using the full-potential projected augmented wave method²⁹ as implemented in the VASP package.³⁰ The spin–orbit coupling (SOC) was included self-consistently. An indirect band gap of ~ 0.81 eV is obtained for $2H$ -MoTe₂ between the valence band maximum at Γ point and conduction band minimum at the center of Γ -K, which is consistent with the transport measurement results. All of the bands are found to be spin degenerate due to the spatial inversion symmetry. The Mo-4d states dominate the energy band from E_F to approximately -1.0 eV, whereas the Te-5p states are of lower energy. It is noteworthy that the valence band energy splitting at K point is primarily due to the SOC instead of the interlayer interaction (Figure 3(a)), which is similar to that found in $2H$ -MoS₂ and $2H$ -WS₂.³¹

The electronic structure of $1T'$ -MoTe₂ (Figure 3(b)) is dramatically different from that of $2H$ -MoTe₂. The finite density of states (DOS) at E_F indicates a metallic phase, and this result is consistent with a metallic behavior of resistivity as shown in Figure 8. The orbital characters around E_F are mainly derived from Mo-4d and Te-5p orbitals. Mo electron-like and Te hole-like band edges cross each other near E_F , which results in a band inversion and being gapped due to SOC. Hence, even though $1T'$ -MoTe₂ has a metallic ground state, the valence band remains separated from the conduction band by a continuous energy gap throughout the entire BZ in the presence of SOC (below, Figure 3(b)). The band inversion feature and well-defined energy gap implies that $1T'$ -MoTe₂ might be characterized as a Z_2 topological insulator (below, Figure 3(b)).¹⁵

The third structure of MoTe₂ is orthorhombic Td phase. Contrary to monoclinic $1T'$ -MoTe₂ phase that possesses spatial inversion symmetry, the crystal inversion symmetry has been broken in Td -MoTe₂, which results from slight lattice structure distortion. Figure 3(c) shows the band structure of Td -MoTe₂ with SOC. The electronic structure exhibits significant band splitting due to the breaking of spatial inversion symmetry except for the time-reversal invariant points. Similar to the $1T'$ phase, Td -MoTe₂ shows a metallic ground state, whereas the orbital characters around E_F are mainly contributed from Mo-4d and Te-5p orbitals. Zooming in around E_F along Γ -X (below, Figure 3(c)) shows that two singly generated bands cross each other and form two Weyl nodes with opposite chirality, which is consistent with a recent theoretical prediction.¹⁸

The scanning transmission electron microscopy (STEM) images of $2H$ -MoTe₂ and $1T'$ -MoTe₂ were obtained in 200 kV JEOL 2100F equipped with a probe corrector for the spherical aberration. The TEM specimens were prepared by mechanical exfoliation and ion beam thinning (Gatan Precision Ion Polishing System II, PIPS II). Figure 4(a) is the high-angle annular dark-field (HAADF) STEM image of $2H$ -MoTe₂ along the $[0001]$ zone axis. The intensity of the HAADF-STEM image is sensitively proportional to the atomic number Z ,^{1,7} so that the positions of Mo atoms appear brighter in the figure. From the selected-area diffraction pattern (inset of Figure 4(a)), the $(\bar{1}\bar{1}00)$ lattice planes are labeled, and the plane spacing is found to be near 3.0 Å, which is consistent with the $2H$ -MoTe₂ hexagonal lattice structure of lattice constant $a = 3.52$ Å. The HAADF-STEM image of the $1T'$ -MoTe₂ phase is shown in Figure 4(b) along the $[001]$ zone axis. The (100) and

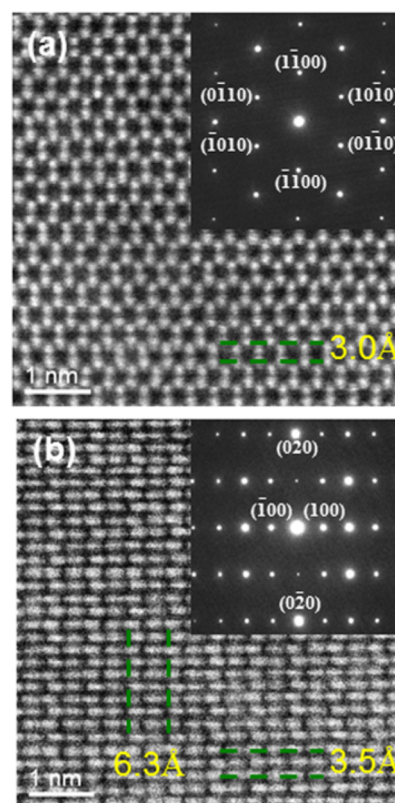


Figure 4. High-angle annular dark-field scanning transmission electron microscopy (HAADF-STEM) images for (a) $2H$ -MoTe₂ and (b) $1T'$ -MoTe₂. The selected-area diffraction pattern for (a) is along the $[0001]$ zone axis and the $[001]$ zone axis for (b). The plane spacing and the lattice planes are labeled.

(010) lattice plane spacings, as labeled in the figure, are consistent with the lattice constants of $a = 6.33$ Å and $b = 3.48$ Å for the $1T'$ -MoTe₂ phase.

The scanning tunneling microscopy (STM) measurements were performed for both $2H$ -MoTe₂ and Td -MoTe₂ at 4.5 K and $1T'$ -MoTe₂ at room temperature using an Omicron LT-STM and an electrochemically etched tungsten tip. dI/dV curves were acquired using the lock-in technique with a bias modulation of 10 mV. Crystals for STM measurements were prepared by in vacuo cleavage at room temperature in a preparation chamber at a base pressure lower than 1×10^{-10} mbar before transfer to an STM chamber with a base pressure lower than 5×10^{-11} mbar. Figure 5 shows atomically resolved topography images taken on (a,b) $2H$ -MoTe₂, (c, d) Td -MoTe₂, and (f, g) $1T'$ -MoTe₂ crystals and the relationship between the observed atomic corrugations of Te surface layer and the corresponding Te surface lattice modeling. The topography for the $2H$ structure exhibits a clear hexagonal surface lattice, whereas the Td and $1T'$ structures have rectangular surface lattices that are indistinguishable using STM topography imaging, which can only probe the uppermost atomic layer and cannot discern the difference in angle β between the two structures. Tunneling spectroscopy curves acquired at 4.5 K as shown in Figure 5(e) suggest a metallic behavior for the Td -MoTe₂ surface, which is consistent with the band structure calculation of apparent n-type, on the other hand, the $2H$ -MoTe₂ surface shows a band gap of around 1.13 eV. These results are consistent with the calculation shown above and with previous predictions.⁹ Interestingly, a

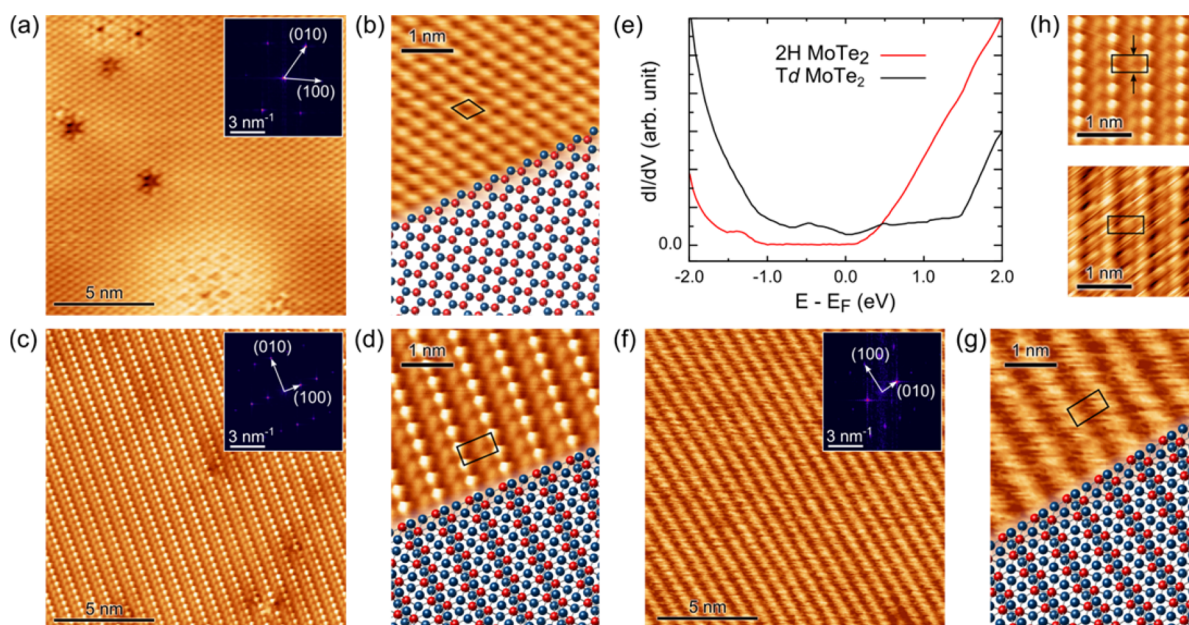


Figure 5. STM and STS measurement results on vacuum-cleaved $2H$ -, Td -, and $1T'$ - MoTe_2 acquired with $V_{\text{bias}} = 0.6$ V and $I = 0.15$ nA. Atomically resolved STM on $2H$ - MoTe_2 , acquired at 4.5 K, is shown in (a) along with the corresponding FFT (inset). An enhanced image displaying the correspondence between the STM image and the Te surface lattice is shown in (b). The corresponding images for Td - MoTe_2 , obtained with $V_{\text{bias}} = -0.1$ V and $I = 0.2$ nA at 4.5 K are shown in (c) and (d), respectively. dI/dV (V) acquired at 4.5 K for $2H$ - and Td - MoTe_2 are shown in (e). An STM topography image acquired for $1T'$ - MoTe_2 (same sample as in (c) and (d) at 294 K) is shown in (f) with its FFT shown in the inset. An enhanced image showing the correspondence to the $1T'$ MoTe_2 lattice is shown in (g). A side-by-side comparison of atomic scale topography of Td - MoTe_2 taken at 4.5 and 77 K is shown in (h) with the features possibly caused by Umklapp interference at 4.5 K marked by black arrows.

comparison of enhanced STM topography of Td - MoTe_2 taken at 4.5 and 77 K, as shown in Figure 5(h), reveals clear protrusions seen at the unit cell edges at 4.5 K (marked by black arrows), which are absent at 77 K. This difference is consistent with a similar one recently observed in WTe_2 , which has been attributed to the onset at low temperature of Umklapp interference of quasiparticles induced by Rashba-type splitting.³² Therefore, the topography at 77 K is expected to better represent the true surface lattice.

Step edges were observed in the as-cleaved MoTe_2 surfaces, as shown in Figure 6, which is helpful to probe the interlayer stacking by exploring the relative orientations of two adjacent MoTe_2 trilayers in stack, as illustrated in Figure 6(b and d). It has been nearly impossible to distinguish the reversed orientation of MoTe_6 units in either trigonal prismatic or octahedral coordination via the surface Te alone, mostly because the Te monolayer on the surface is always arranged in hexagonal close packing. However, we might distinguish the reversed orientation by taking advantage of the different local geometries for the Te vacancy defect sitting on surfaces of reversed orientation. Two types of characteristic defects can be identified in $2H$ - MoTe_2 and Td - MoTe_2 at 4.5 K (Figure 6), as indicated by the dark arrowhead-like defects of symmetry m for Td - MoTe_2 , and the bright three-lobed defects of symmetry $3m$ for $2H$ - MoTe_2 . In particular, the orientations for the two types of defects are seen reversed from one region to the next region that is one trilayer below, which is consistent with the $2H$ ($P6_3/mmc$) and Td ($Pmn2_1$) symmetries of required reverse orientation between neighboring layers. Although $2H$ - MoTe_2 is able to maintain its hexagonal symmetry per layer, Td - MoTe_2 has lost its hexagonal symmetry with the additional in-plane mirror symmetry breaking (Figure 2), which is consistently reflected on the observed defect local symmetry of reversed orientations between neighboring layers exposed to the surface,

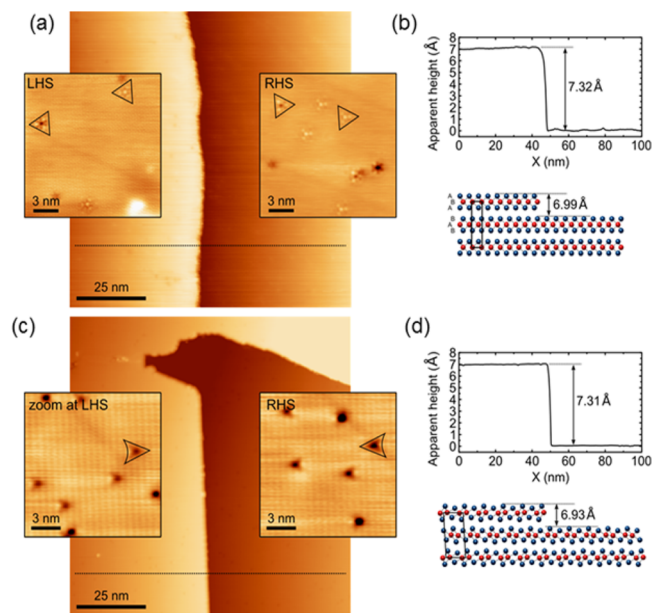


Figure 6. Stacking of trilayers in $2H$ - and Td - MoTe_2 at 4.5 K. (a) Large-scale STM topography map ($V_{\text{bias}} = 1$ V, $I = 0.3$ nA), including a single trilayer step-edge and enhanced images (insets, $V_{\text{bias}} = 1$ V, $I = 0.3$ nA) taken on its left- and right-hand sides, showing a reversal of orientation of the characteristic dark arrowhead-shaped defects located in the two adjacent trilayers. (b) Topographic line profile taken across the step edge (along the dashed line in the large scale map), showing a height comparable with half the c -axis lattice parameter. The corresponding STM topography images ($V_{\text{bias}} = -1$ V, $I = 0.2$ nA) for both the large-scale and enhanced images) and line profile for the $1T'$ structure (c and d), also revealing a reversal of orientation for the bright three-lobed defects (bound by black triangles) in the two adjacent trilayers.

i.e., the former has the three-lobe shape of $3m$ symmetry and the latter has the arrowhead-like shape of m symmetry only.

The $2H$ and $1T'$ phases of MoTe_2 of various thicknesses have been characterized with Raman spectroscopy at room temperature, as shown in Figure 7. The $2H$ - MoTe_2 crystal shows

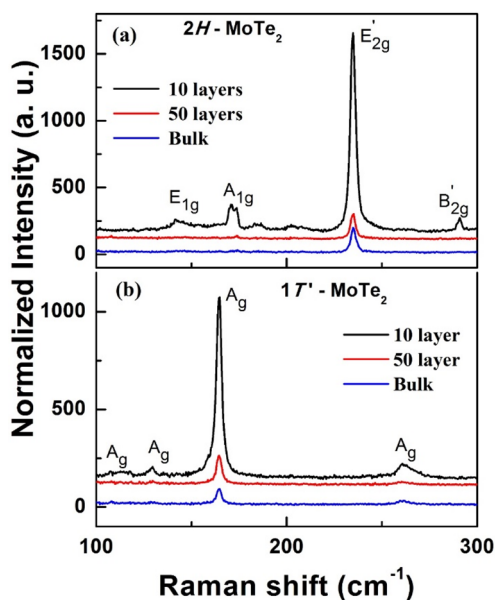


Figure 7. Room-temperature Raman spectra for (a) $2H$ - MoTe_2 and (b) $1T'$ - MoTe_2 with various layer thicknesses.

Raman peaks between 100 and 300 cm^{-1} (Figure 7(a)), including the prominent peak of the in-plane E_{2g}^1 mode at $\sim 234\text{ cm}^{-1}$, the out-of-plane A_{1g} mode at $\sim 173\text{ cm}^{-1}$, and the out-of-plane bulk inactive B_{2g}^1 phonon mode ($\sim 290\text{ cm}^{-1}$). The intensity of the Raman modes shows significant thickness dependence from the bulk sample to the nanothickness near ~ 10 layers. The presence of B_{2g}^1 mode in the 10-layers sample indicates that the synthesized sample is atomically thin. Besides the observed first-order Raman peaks, several second-order resonant peaks with relatively low intensities at ~ 144 , 183 , and 204 cm^{-1} are also observed in $2H$ - MoTe_2 . The observed characteristic peaks of $1T'$ - MoTe_2 are A_g (108.2 cm^{-1}), A_g (129.2 cm^{-1}), A_g (164.8 cm^{-1}), and A_g (261.5 cm^{-1}), as shown in Figure 7(b). Furthermore, a peak related to the Raman mode (B_g) at 180 cm^{-1} was observed at room temperature,³³ whereas this mode disappeared at low temperature, as shown in Figure S3, which could be related to the expected $1T'$ to Td phase transition near $\sim 240\text{ K}$. The observed phonon modes match with those reported in the literature,^{33–40} and the phase purities for both phases are confirmed in addition to the XRD structural analysis (Figure 1). The most prominent peak for $2H$ - MoTe_2 is 234 cm^{-1} corresponding to the E_{2g} phonon, in contrast to 166 cm^{-1} corresponding to the A_g phonon for $1T'$ - MoTe_2 , which is consistent with the expected easier excitation for Te atoms in the distorted trilayer along the c -direction for the latter.³⁵

The electrical resistivities $\rho(T)$ as a function of temperature for both $1T'$ - and $2H$ - MoTe_2 are shown in Figure 8. Figure 8(a) shows the resistivity of $2H$ - MoTe_2 as a function of temperature; a slight decrease upon cooling from 300 to 160 K is observed and then increases at lower temperature, which suggests the existence of a thermally excitable narrow gap of

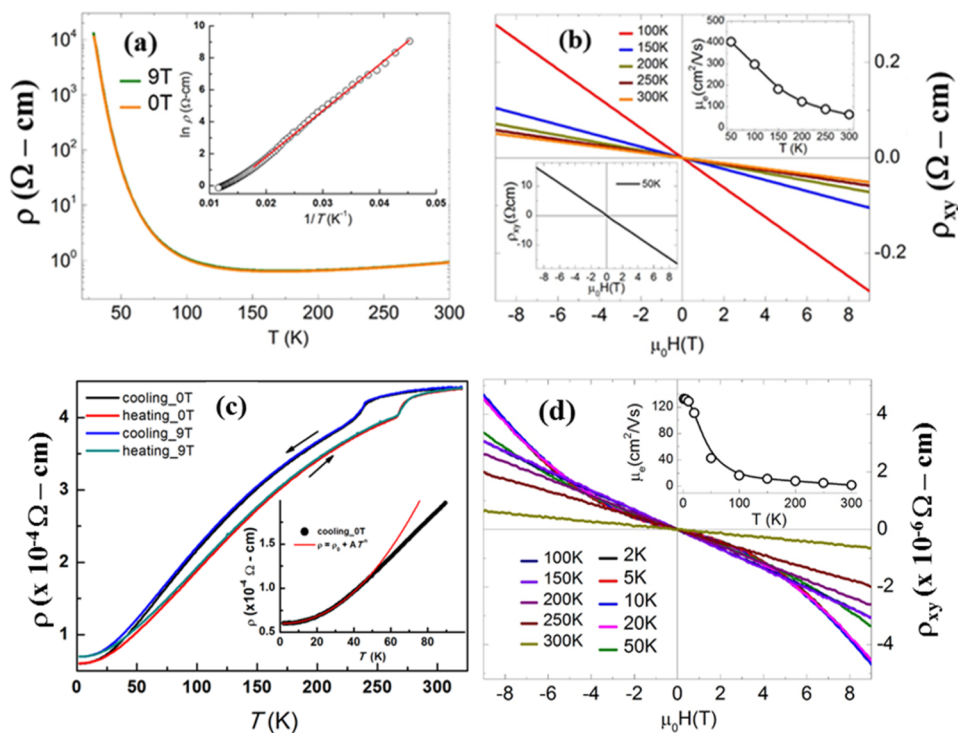


Figure 8. (a) Resistivity of $2H$ - MoTe_2 as a function of temperature. Inset shows the Arrhenius behavior below 50 K of a fitted gap size of $\sim 35.3\text{ meV}$. (b) Hall resistivity of $2H$ - MoTe_2 as a function of magnetic field at different temperatures (50 K data are displayed in the lower left corner in larger scale). The temperature dependence of Hall mobility is shown in the inset. (c) Resistivity of $1T'$ - MoTe_2 as a function of temperature. Inset presents the fitting result according to the Fermi liquid theory (red solid line). (d) Hall resistivity of $1T'$ - MoTe_2 as a function of magnetic field at different temperatures with temperature dependence of Hall mobility displayed in the inset.

35.3 meV fitted with an Arrhenius law below 50 K (inset of Figure 8(a)). Further, we also fit the data to the variable range hopping mechanism $\rho = \rho_0 \exp(T_0/T)^{1/3}$ for two dimensions and found the hopping parameter ($T_0^{1/3}$) to be equal to 80 K^{1/3}. This gives rise to a differential activation energy of 31 meV at 50 K. Activation energy obtained from both mechanisms is on the same order. Figure 8(b) shows the Hall resistivity ρ_{xy} at several temperatures for the 2H-MoTe₂ single crystal. ρ_{xy} data shows a good linearity relative to the magnetic field up to 9 T above 50 K, indicating the dominance of electron carriers. Electronic mobility decreases with rising temperature (inset of Figure 8(b)) of ~ 400 cm² V⁻¹ s⁻¹ at 50 K. Because the band gap size of the ideal 2H-MoTe₂ has been estimated to be near ~ 1.0 eV (Figure 3), it is possible that the identified narrow gap from the transport study is the gap between the impurity and the conduction bands of n-type doping introduced by Te vacancies.²¹ The magnetic field of 9 T does not affect the resistivity behavior with apparently no magnetoresistance.

The $\rho(T)$ curve of 1T'-MoTe₂ indicates a metallic behavior of $\sim 4.4 \times 10^{-4}$ Ω cm at room temperature as shown in Figure 8(c). A hysteretic anomaly in resistivity is observed between 240 and 265 K upon the warming and cooling cycles, which has been assigned corresponding to a first-order structural phase transition from the 1T' phase to a low-temperature orthorhombic Td phase.¹⁴ This 1T'-to-Td phase transition can also be identified in the magnetic susceptibility and specific heat measurements, as shown in Figures S4 and S5. The magnetic susceptibilities of single crystal 1T'-MoTe₂ as a function of temperature were measured in an applied magnetic field of 10 kOe for field applied along the *ab*-direction, and a hysteretic $\chi(T)$ step type anomaly near ~ 254 K is found. In addition, the heat capacity $C_p(T)$ shows an anomaly of onset near ~ 250 K. Fitting C_p with the electronic and phonon contributions in $C_p/T = \gamma + \beta T^2$, where γ is the normal-state electronic contribution and β is the lattice contribution to the specific heat, the fitted results yield $\gamma = 3.22$ mJ mol⁻¹ K⁻² and $\beta = 0.849$ mJ mol⁻¹ K⁻⁴ for Td-MoTe₂. Considering the saturation value (74.93 J mol⁻¹ K⁻¹ at 300 K) as the Debye–Pettit classical limit, the derived Debye temperature ($\beta = N(12/S)\pi^4 R \Theta_D^{-3}$ ($R = 8.314$ J mol⁻¹ K⁻¹) is found to be 190 K, which is of the same order and consistent with that found in orthorhombic WTe₂.⁴¹

The $\rho(T)$ behavior does not show any noticeable change under a 9 T magnetic field for both 1T'-MoTe₂ and Td-MoTe₂ (Figure 8(c)), which is surprising compared to WTe₂ (orthorhombic Td structure) being identified as a large magnetoresistance material due to perfect electron and hole compensation.⁵ Such a compensation of electron and holes are absent in Td-MoTe₂.²⁰ The low temperature part ($T < 50$ K) of the $\rho(T)$ data is well fitted by $\rho(T) = \rho_0 + AT^2$ following the Fermi liquid model, as shown by the solid red line in the inset of Figure 8(c). The obtained fitting parameters are the residual resistivity $\rho_0 = 5.97 \times 10^{-5}$ Ω cm and coefficient $A = 1.42 \times 10^{-8}$ Ω cm K⁻², which indicates the Fermi liquid-like behavior for Td-MoTe₂ single crystal below 50 K.⁴² In semimetals like 1T'MoTe₂, the temperature-dependent resistivity can be expressed as $\rho = a + bT + cT^2$, where the first term is from electron-defect scattering, the second term is electron–electron scattering, and the third term is electron–phonon scattering. At low temperature, because of negligible phonon contribution, the resistivity varies almost as T^2 , commonly known as the Fermi liquid behavior. At higher temperature, although the T^2

term is present, because of large phonon contribution (large value of coefficient b), the resistivity varies almost linearly. The ρ_{xy} as a function of magnetic field at different temperatures for 1T'-MoTe₂ (at $T = 300$ K) and Td-MoTe₂ (below 260 K) is shown in Figure 8(d). Below 260 K, ρ_{xy} shows a nonlinear behavior with magnetic field for the Td-MoTe₂ single crystal. Electrons remain the majority charge carriers in the whole temperature range for both 1T'-MoTe₂ and Td-MoTe₂ single crystals. Td-MoTe₂ has an electron mobility of 133 cm² V⁻¹ s⁻¹ at 2 K and decreases with increasing temperature, whereas electron mobility of 1T'-MoTe₂ is very small at the level of ~ 3 cm² V⁻¹ s⁻¹ at 300 K (inset of Figure 8(d)). The decrease in the carrier mobility of both 2H and 1T' forms of MoTe₂ decreases with temperature. This is very common in metals and semiconductors. This is mostly due to the increased phonon density at higher temperatures, which results in the smaller τ (average interval between two scattering events). As mobility is directly related to τ ($\mu = q\tau/m^*$, where q is the electronic charge and m^* is the effective mass), mobility also decreases with temperature. The effect of the phonon can easily be seen in the resistivity in metals. In 1T'-MoTe₂, due to the negligible electron–phonon scattering contribution at low temperature, the rate of decrease in resistivity decreases and almost saturates. Interestingly, the mobility also saturates at low temperature and decreases thereafter upon increasing temperature. These transport properties are consistent with those estimated from tunneling spectroscopy of STM shown in Figure 5.

CONCLUSIONS

Large and high-quality single crystals of layered MoTe₂ in both 2H- and 1T'-types have been grown using a CVT method, and the low temperature Td phase can also be generated from the as-grown 1T'-MoTe₂. The three phases of distinctly different layer structures have been confirmed rigorously with XRD, Raman spectroscopy, STEM, and STM studies. The physical properties have also been compared through electrical resistivity, magnetic susceptibility, and specific heat measurements. Scanning tunneling spectroscopy confirms the reversed stacking relationship between the adjacent MoTe₂ trilayers via the local symmetry of the point defects. The metallic behavior of Td-MoTe₂ is found to be consistent with the predicted Weyl semimetal phase, and the n-type semiconducting behavior for 2H-MoTe₂ has also been confirmed via resistivity and STM tunneling spectroscopy.

ASSOCIATED CONTENT

Supporting Information

The Supporting Information is available free of charge on the ACS Publications website at DOI: 10.1021/acs.chemmater.6b04363.

Crystal growth profiles, refined room-temperature SXRD patterns, Raman spectra for 1T'-MoTe₂ single crystals with various temperatures, magnetic susceptibilities, and heat capacity data (PDF)

AUTHOR INFORMATION

Corresponding Authors

*E-mail: sankarndf@gmail.com, sankarraman@gate.sinica.edu.tw.

*E-mail: fcchou@ntu.edu.tw.

ORCID

Raman Sankar: 0000-0003-4702-2517

Notes

The authors declare no competing financial interest.

ACKNOWLEDGMENTS

R.S. and F.C.C. acknowledge the support provided by the Academia Sinica research program on Nanoscience and Nanotechnology under project number NM004. F.C.C. acknowledges support from the Ministry of Science and Technology in Taiwan under project number MOST-102-2119-M-002-004. We thank the Nanoscience and Technology thematic research program of Academia Sinica, Taiwan.

REFERENCES

- (1) Sipoš, B.; Kusmartseva, A. F.; Akrap, A.; Berger, H.; Forró, L.; Tutiš, E. From Mott state to superconductivity in 1T-TaS₂. *Nat. Mater.* **2008**, *7*, 960–965.
- (2) Ang, R.; Wang, Z. C.; Chen, C. L.; Tang, J.; Liu, N.; Liu, Y.; Lu, W. J.; Sun, Y. P.; Mori, T.; Ikuhara, Y. Atomistic origin of an ordered superstructure induced superconductivity in layered chalcogenides. *Nat. Commun.* **2015**, *6*, 6091–6096.
- (3) Mak, K.; Lee, C.; Hone, J.; Shan, J.; Heinz, T. F. A New Direct-Gap Semiconductor. *Phys. Rev. Lett.* **2010**, *105*, 136805–136808.
- (4) Chen, K. X.; Wang, X. M.; Mo, D. C.; Lyu, S. S. Thermoelectric Properties of Transition Metal Dichalcogenides: From Monolayers to Nanotubes. *J. Phys. Chem. C* **2015**, *119*, 26706–26711.
- (5) Ali, M. N.; Xiong, J.; Flynn, S.; Tao, J.; Gibson, Q. D.; Schoop, L. M.; Liang, T.; Haldolaarachchige, N.; Hirschberger, M.; Ong, N. P.; Cava, R. J. Large, non-saturating magnetoresistance in WTe₂. *Nature* **2014**, *514*, 205–208.
- (6) Thoutam, L. R.; Wang, Y. L.; Xiao, Z. L.; Das, S.; Luican-Mayer, A.; Divan, R.; Crabtree, G. W.; Kwok, W. K. Temperature-Dependent Three-Dimensional Anisotropy of the Magnetoresistance in WTe₂. *Phys. Rev. Lett.* **2015**, *115*, 046602–046606.
- (7) Castro Neto, C.; Novoselov, K. Two-Dimensional Crystals: Beyond Graphene. *Mater. Express* **2011**, *1*, 10–17.
- (8) Radisavljevic, B.; Radenovic, A.; Brivio, J.; Giacometti, V.; Kis, A. Single-layer MoS₂ transistors. *Nat. Nanotechnol.* **2011**, *6*, 147–150.
- (9) Soluyanov, A. A.; Gresch, D.; Wang, Z.; Wu, Q. S.; Troyer, M.; Dai, X.; Bernevig, B. A. Type-II Weyl semimetals. *Nature* **2015**, *527*, 495–498.
- (10) Podberezskaya, N. V.; Magarill, S. A.; Pervukhina, N. V.; Borisov, S. V. Crystal Chemistry of Dichalcogenides MX₂. *J. Struct. Chem.* **2001**, *42*, 654–681.
- (11) Ataca, C.; Şahin, H.; Ciraci, S. Transition-Metal Oxides and Dichalcogenides in a Honeycomb-Like Structure. *J. Phys. Chem. C* **2012**, *116*, 8983–8999.
- (12) Brown, B. E. The crystal structures of WTe₂ and high-temperature MoTe₂. *Acta Crystallogr.* **1966**, *20*, 268–274.
- (13) Puotinen, D.; Newnham, R. E. The crystal structure of MoTe₂. *Acta Crystallogr.* **1961**, *14*, 691–692.
- (14) Hughes, H. P.; Friend, R. H. Electrical resistivity anomaly in β-MoTe₂ (metallic behavior). *J. Phys. C: Solid State Phys.* **1978**, *11*, L103–L105.
- (15) Qian, X.; Liu, J.; Fu, L.; Li, J. Quantum spin Hall effect in two-dimensional transition metal dichalcogenides. *Science* **2014**, *346*, 1344–1347.
- (16) Levy, F. A. *Intercalated Layered Materials*; D. Reidel Publishing: Dordrecht, Holland, 1979.
- (17) Chang, T.-R.; Xu, S.-Y.; Chang, G.; Lee, C.-C.; Huang, S.-M.; Wang, B. K.; Bian, G.; Zheng, H.; Sanchez, D. S.; Belopolski, I.; Alidoust, N.; Neupane, M.; Bansil, A.; Jeng, H.-T.; Lin, H.; Zahid Hasan, M. Prediction of an arc-tunable Weyl Fermion metallic state in Mo_xW_{1-x}Te₂. *Nat. Commun.* **2016**, *7*, 10639–9.
- (18) Sun, Y.; Wu, S.-C.; Ali, M. N.; Felser, C.; Yan, B. Prediction of Weyl semimetal in orthorhombic MoTe₂. *Phys. Rev. B: Condens. Matter Mater. Phys.* **2015**, *92*, 161107-1–161107-7.
- (19) Clarke, R.; Marseglia, E.; Hughes, H. P. A low-temperature structural phase transition in β-MoTe₂. *Philos. Mag. B* **1978**, *38*, 121–126.
- (20) Keum, D.; Cho, S.; Kim, V.; Choe, D.-H.; Sung, H.-J.; Kan, M.; Kang, H.; Hwang, J.-Y.; Kim, S. W.; Yang, H.; Chang, K. J.; Lee, Y. H. Bandgap opening in few-layered monoclinic MoTe₂. *Nat. Phys.* **2015**, *11*, 482–486.
- (21) Vellinga, M. B.; de Jonge, R.; Haas, C. Semiconductor to metal transition in MoTe₂. *J. Solid State Chem.* **1970**, *2*, 299–302.
- (22) Wieting, T. J. Electrical conductivity of thin single crystals of the IVB-VIB dichalcogenides. *J. Phys. Chem. Solids* **1970**, *31*, 2148–2151.
- (23) Al-Hilli, A. A.; Evans, B. L. The preparation and properties of transition metal dichalcogenide single crystals. *J. Cryst. Growth* **1972**, *15*, 93–101.
- (24) Bromley, R. A.; Murray, R. B.; Yoffe, A. D. The band structures of some transition metal dichalcogenides: III. Group VIA: trigonal prism materials. *J. Phys. C: Solid State Phys.* **1972**, *5*, 759–778.
- (25) Davey, B.; Evans, H. L. The optical properties of MoTe₂ and WSe₂. *Phys. Status. Solidi (a)*. *Phys. Status. Solidi (a)* **1972**, *13*, 483–491.
- (26) Wilson, J. A.; Yoffe, A. D. The transition metal dichalcogenides discussion and interpretation of the observed optical, electrical and structural properties. *Adv. Phys.* **1969**, *18*, 193–335.
- (27) Dawson, W. G.; Bullett, D. W. Electronic structure and crystallography of MoTe₂ and WTe₂. *J. Phys. C: Solid State Phys.* **1987**, *20*, 6159–6174.
- (28) Perdew, J. P.; Burke, K.; Ernzerhof, M. Generalized Gradient Approximation Made Simple. *Phys. Rev. Lett.* **1996**, *77*, 3865–3868.
- (29) Blochl, P. E. Projector augmented-wave method. *Phys. Rev. B: Condens. Matter Mater. Phys.* **1994**, *50*, 17953–17979. Kresse, G.; Joubert, J. From ultrasoft pseudopotentials to the projector augmented-wave method. *Phys. Rev. B: Condens. Matter Mater. Phys.* **1999**, *59*, 1758–1775.
- (30) Kresse, G.; Hafner, J. Ab initio molecular dynamics for open-shell transition metals. *Phys. Rev. B: Condens. Matter Mater. Phys.* **1993**, *48*, 13115–13118. Kresse, G.; Furthmüller, J. Efficiency of ab-initio total energy calculations for metals and semiconductors using a plane-wave basis set. *Comput. Mater. Sci.* **1996**, *6* (6), 15–50.
- (31) Latzke, D. W.; Zhang, W.; Suslu, A.; Chang, T.-R.; Lin, H.; Jeng, H.-T.; Tongay, S.; Wu, J.; Bansil, A.; Lanzara, A. Electronic structure, spin-orbit coupling, and interlayer interaction in bulk MoS₂ and WS₂. *Phys. Rev. B: Condens. Matter Mater. Phys.* **2015**, *91*, 235202-1–235202-6.
- (32) Li, Q.; Yan, J.; Yang, B.; Zang, Y.; Zhang, J.; He, K.; Wu, M.; Zhao, Y.; Mandrus, D.; Wang, J.; Xue, Q.; Chih, L.; Singh, D. J.; Pan, M. Interference evidence for Rashba-type spin-split on semimetallic WTe₂ surface; arXiv:1602.08256v1 [cond-mat.mtrl-sci], 2016.
- (33) Park, J. C.; Yun, S. J.; Kim, H.; Park, J. H.; Chae, S. H.; An, S. J.; Kim, J. G.; Kim, S. M.; Kim, K. K.; Lee, Y. H. Phase-Engineered Synthesis of Centimeter-Scale 1T' and 2H-Molybdenum Ditelluride Thin Films. *ACS Nano* **2015**, *9*, 6548–6554.
- (34) Lin, Y.-F.; Xu, Y.; Wang, S.-T.; Li, S.-L.; Yamamoto, M.; Aparecido-Ferreira, A.; Li, W.; Sun, H.; Nakaharai, S.; Jian, W.-B.; Ueno, K.; Tsukagoshi, K. Ambipolar MoTe₂ Transistors and Their Applications in Logic Circuits. *Adv. Mater.* **2014**, *26*, 3263–3269.
- (35) Cho, S.; Kim, S.; Kim, J. H.; Zhao, J.; Seok, J.; Keum, D.; Baik, J.; Choe, D.-H.; Chang, K. J.; Suenaga, K.; Kim, S. W.; Lee, Y. H.; Yang, H. Phase patterning for ohmic homojunction contact in MoTe₂. *Science* **2015**, *349*, 625–628.
- (36) Joshi, J.; Stone, I.; Beams, R.; Krylyuk, S.; Kalish, I.; Davydov, A.; Vora, P. Phonon Anharmonicity in Bulk Td-MoTe₂. *Appl. Phys. Lett.* **2016**, *109*, 031903–031907.
- (37) Chen, S. Y.; Goldstein, T.; Venkataraman, D.; Ramasubramaniam, A.; Yan, J. Activation of New Raman Modes by Inversion Symmetry Breaking in Type II Weyl Semimetal Candidate T'-MoTe₂. *Nano Lett.* **2016**, *16*, 5852–5860.
- (38) Beams, R.; Cañado, L. G.; Krylyuk, S.; Kalish, I.; Kalanyan, B.; Singh, A. K.; Choudhary, K.; Bruma, A.; Vora, P. M.; Tavazza, F.; Davydov, A. V.; Stranick, S. J. Characterization of Few-Layer 1T'

MoTe₂ by Polarization-Resolved Second Harmonic Generation and Raman Scattering. *ACS Nano* **2016**, *10*, 9626–9636.

(39) Zhang, K.; Bao, C.; Gu, Q.; Ren, X.; Zhang, H.; Deng, K.; Wu, Y.; Li, Y.; Feng, J.; Zhou, S. *Raman signatures of inversion symmetry breaking and structural phase transition in type-II Weyl semimetal MoTe₂*; arXiv:1606.05071, 2016. <https://arxiv.org/abs/1606.05071>.

(40) Naylor, C. H.; Parkin, W. M.; Ping, J.; Gao, Z.; Zhou, Y. R.; Kim, Y.; Streller, F.; Carpick, R. W.; Rappe, A. M.; Drndic, M.; Kikkawa, J. M.; Johnson, A. T. C. Monolayer Single-Crystal 1T'-MoTe₂ Grown by Chemical Vapor Deposition Exhibits Weak Antilocalization Effect. *Nano Lett.* **2016**, *16*, 4297–4304.

(41) Callanan, J. E.; Hope, G. A.; Weir, R. D.; Westrum, E. F., Jr. The preparation and lowtemperature heat capacity at temperatures from 6 to 326 K. *J. Chem. Thermodyn.* **1992**, *24*, 627–638.

(42) Zandt, T.; Dwelk, H.; Janowitz, C.; Manzke, R. Quadratic temperature dependence up to 50 K of the resistivity of metallic MoTe₂. *J. Alloys Compd.* **2007**, *442*, 216–218.